8-7-2011

In Situ Synthesis of Ultrafine ß-MnO_2/Polypyrrole Nanorod Composites for High-Performance Supercapacitors

Jianfeng Zang

Xiaodong Li
University of South Carolina - Columbia, lixiao@cec.sc.edu

Publication Info

Published in *Journal of Materials Chemistry*, Volume 21, Issue 29, 2011, pages 10965-10969.

This article was first published by the Royal Society of Chemistry and can be found at http://dx.doi.org/10.1039/C1JM11491C
Zang, J & Li, X. (7 August 2011). *In Situ* Synthesis of Ultrafine ß-MnO_2/Polypyrrole Nanorod Composites for High-Performance Supercapacitors. Journal of Materials Chemistry, 21 (29), 10965 – 10969. http://dx.doi.org/10.1039/C1JM11491C

Journal of Materials Chemistry

Cite this: *J. Mater. Chem.*, 2011, **21**, 10965

www.rsc.org/materials

PAPER

In situ synthesis of ultrafine β-MnO_2/polypyrrole nanorod composites for high-performance supercapacitors

Jianfeng Zang and Xiaodong Li*

Received 8th April 2011, Accepted 11th May 2011
DOI: 10.1039/c1jm11491c

We report a remarkable observation that is at odds with the established notion that β-MnO_2 was regarded as an undesirable candidate for supercapacitor applications. The specific capacitance of β-MnO_2 can reach as high as 294 F g^{-1}, which is comparable to the best crystallographic structure, like α-MnO_2. The key is to substantially decrease the size of β-MnO_2 powders to ultra small regime. We demonstrate a facile, simple, and effective approach to synthesizing ultrafine (<10 nm in diameter) β-MnO_2/polypyrrole nanorod composite powders for high-performance supercapacitor electrodes. Our observation may encourage a revisit of the other good or even bad candidate active materials if we can decrease their size to extremely small scales. In addition, the proposed synthetic mechanism and the developed synthetic strategy may provide design guidelines in synthesizing other energy storage materials toward ultrafine 1D nanostructures.

Introduction

Supercapacitors have been extensively studied as the most promising candidates for next-generation energy storage systems. With combined characteristics of both high energy density and high power density, supercapacitors have been used in numerous applications, such as starters, power back-up systems, and hybrid electrical vehicles.[1,2] Many materials have been investigated as the electrode materials in supercapacitors, including carbon, conducting polymers, and both noble and transition-metal oxides.[1–5] MnO_2 has attracted tremendous research interest due to its low cost, high energy density, and environmental friendliness.[6] A theoretical capacitance as high as 1233 F g^{-1} was reported for MnO_2 when a total reduction of Mn (IV) to Mn(III) occurred for a one electron transfer per manganese atom over 0.9 V potential window.[7] However, like other transition metal oxide materials, the high specific capacitance potential of manganese oxide is hindered by its limited electrode kinetics, where only a very outside surface thin layer participates in the charge-storage process and the rest of the material remains inactive.[8–10] Efforts on coating a thin layer of amorphous MnO_2 on nanowires to realize a high surface area have successfully boosted the specific capacitance of this active material very close to its theoretical potential.[11,12] Despite the great potential application of thin films in microsystems, powders of active materials are required for most practical applications, such as in high-power-density devices.

Department of Mechanical Engineering, University of South Carolina, 300 Main Street, Columbia, South Carolina, 29208, USA. E-mail: lixiao@cec.sc.edu; Fax: +1 803-777 0106; Tel: +1 803-777 8011

Recent research on manganese oxide in various nanostructures as the functional building components for supercapacitors has demonstrated enhanced specific capacitance, high power density, and high rate capability because the nanostructures provide high surface area, short ion diffusion path, and fast kinetics.[11,13–16] Various reports revealed that the higher Brunauer–Emmett–Teller (BET) surface area does not always result in a higher capacitance in crystalline MnO_2.[7,17,18] The capacitance of MnO_2 is strongly dependent on its crystallographic structure and it decreases in the following order: α (297 F g^{-1}) $\approx \delta > \gamma > \lambda > \beta$ ($\sim$7 F g^{-1}).[18] The narrow tunnel size (1.89 Å) of the one dimensional (1D) channel impedes the intercalation of cations in β-MnO_2. Thus, β-MnO_2 has been regarded as the undesirable candidate for supercapacitor applications.

In this work, we report a remarkable observation that is at odds with the established notion. The specific capacitance of β-MnO_2 powder can reach as high as 294 F g^{-1}, which is comparable to the best crystallographic structure, like α-MnO_2, when the size of β-MnO_2 nanorod decreases to ultra small regime, *e.g.*, 5–10 nm in diameter. We demonstrate a facile, one-step, and *in situ* co-precipitation approach to synthesizing ultrafine β-MnO_2/polypyrrole nanorod composite powders at room temperature. In this approach, pyrrole monomers worked as a reduction agent to reduce Mn^{7+} ions in $KMnO_4$ solution to form Mn^{4+} ions in the form of β-MnO_2 crystal; at the same time the pyrrole monomers were subjected to an oxidative polymerization process to form conductive polypyrrole. The *in situ* generated conductive polymer, which sheathed the β-MnO_2 crystal, effectively prevented it from further growing. The structural nature of [MnO_6] octahedra could produce 1D structure products through proper control of the synthetic conditions.[19] The reaction was carefully controlled to form ultrafine nanorods with a diameter down to

5–10 nm and the formation mechanism was discussed in terms of thermal dynamics of crystallization.

Experimental section

Synthesis of ultrafine nanorod composites

All chemical reagents were in analytical grade and used as received. In a typical procedure for the preparation of ultrafine MnO_2/polypyrrole nanorod composite powders, pyrrole (Sigma Aldrich) monomer (0.7 mL) and concentrated H_2SO_4 (0.3 mL) were dissolved in 100 mL deionized (DI) water with stirring. $KMnO_4$ powder (Sigma Aldrich, 2.7 g) was dissolved in 40 mL DI water. The $KMnO_4$ solution was added into the pyrrole solution with vigorous stirring and reacted for 60 min, producing a large amount of black precipitates simultaneously. After washing with sufficient DI water, the precipitates were dried at 90 °C in air for 12 h.

Material characterization

X-Ray diffraction (XRD) analysis was performed on the as-prepared products with a Rigaku D/Max 2100 Powder X-ray Diffractometer with Cu Kα radiation (λ = 1.54 Å) with a diffracted beam graphite monochromator. The morphologies of the prepared products were examined using a field-effect scanning microscope (FESEM, Zeiss Ultra Plus) and a high-resolution transmission electron microscope (HRTEM, JEOL 2100F). The products dispersed in DI water were sonicated for 30 min and then dropped onto a Cu grid having a holey carbon support film for HRTEM observation. FTIR analysis was conducted using a PerkinElmer Spectrum 100 FTIR Spectrometer with a reflection accessory.

Electrochemical characterization

The working electrodes were fabricated by mixing the prepared MnO_2/polypyrrole nanorod composite powders with 15 wt% acetylene black and 5 wt% polytetrafluorene-ethylene (PTFE) binder. A small amount of DI-water was added into the mixture to produce a homogeneous paste. The mixture paste was pressed onto nickel foam current-collectors (1.0 × 1.0 cm) to make electrodes. The loading level of the active materials on the nickel foam is about 2–5 μg cm^{-2}. The prepared electrode was soaked in 1 M Na_2SO_4 solution overnight before the electrochemical test. Electrochemical characterization was carried out in a conventional three-electrode cell with 1 M Na_2SO_4 as the electrolyte. A platinum foil and Ag/AgCl were used as the counter and reference electrode, respectively. All electrochemical measurements were conducted using a CHI 760D electrochemical workstation (CH Instruments Inc., Texas, USA). Specific capacitance was calculated based on active materials of MnO_2/polypyrrole per gram.

Results and discussion

Structure characterization

The synthesized nanocomposite powders were first characterized by X-ray diffraction (XRD). As shown in Fig. 1a, all of the diffraction peaks for the as-prepared sample were indexed with

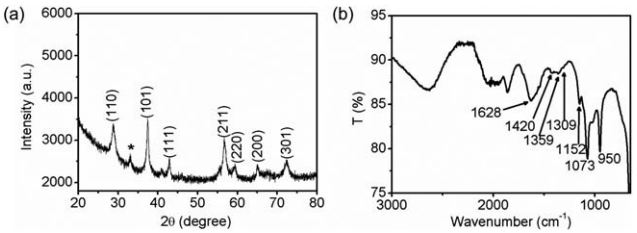

Fig. 1 (a) XRD and (b) FTIR spectra of MnO_2/polypyrrole nanorod composite powders.

the standard XRD pattern of β-MnO_2 (JCPDS No. 24-0735, tetragonal symmetry with *P*42/mnm space group and lattice constants of a = 4.399 nm and c = 2.874 nm). The diffraction peak at 2θ = 33° results from polypyrrole. No characteristic impurity peak is observed, indicating that the high purity MnO_2/polypyrrole composite was produced by the simple co-precipitation method.

The FTIR spectrum of the as-prepared MnO_2/polypyrrole nanorod composite powders is presented in Fig. 1b. The main characteristic peaks of polypyrrole are assigned as follows: the peak at 1628 cm^{-1} is assigned to the vibration of C=C/C–C, while bands at 1420 and 1359 cm^{-1} are attributed to the pyrrole ring vibration.[20–22] The bands located at 1309 and 1152 cm^{-1} are ascribed to the C–H in-plane deformation and the C–N stretching vibrations,[23] while other bands at 1073 and 950 cm^{-1} reflect N–H in-plane deformation vibration and the C–H out-of-plane vibration, respectively, implying the doping state of polypyrrole.[24,25] Our observation of both the difference in peak position and intensity between the as-prepared sample and the pure polypyrrole reported in the literature reflects a mutual interaction between polypyrrole and MnO_2, further indicating that a MnO_2/polypyrrole hybrid composite was formed.

The as-prepared products were further examined by field-effect scanning electron microscopy (FESEM). As shown in Fig. 2a and b, the as-prepared MnO_2/polypyrrole nanorod

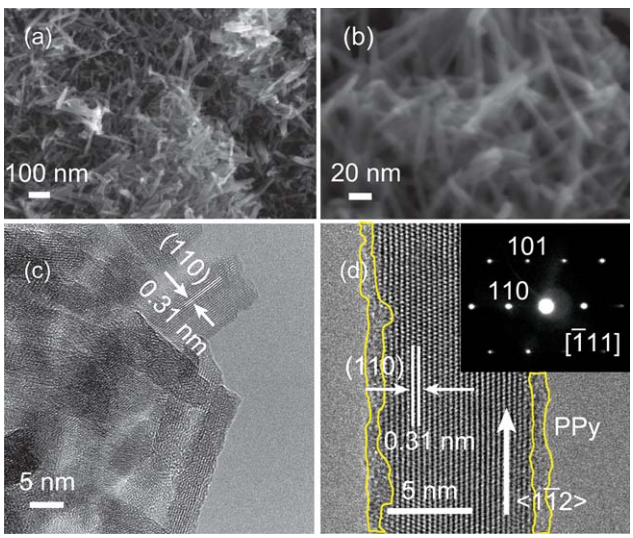

Fig. 2 (a and b) Low- and high-magnification FESEM images of the β-MnO_2/polypyrrole nanorod composite. (c and d) HRTEM analysis. The inset of panel (d) is its corresponding SAED pattern.

composite powders are ultrafine nanorods, 5–10 nm in diameter and 50–200 nm in length.

We also performed high-resolution transmission electron microscopy (HRTEM) examination on the MnO_2/polypyrrole nanorod composite for a more detailed structural analysis. Fig. 2b and c present the MnO_2/polypyrrole composite in the ultrafine rod shape. The lattice fringes are clearly visible with a spacing of 0.31 nm, which is in good agreement with the spacing of the (110) plane of the crystal β-MnO_2. The crystal growth direction of the nanorod is $\langle 1\bar{1}2\rangle$. The inset of Fig. 2d clearly depicts the selected area electron diffraction (SAED) pattern with (110) and (101) crystal planes. The TEM results are consistent with the above XRD results, and further confirm that single crystalline β-MnO_2 has been successfully produced. In a closer examination of the HRTEM image (labelled by yellow lines in Fig. 2d), we observe that an obvious amorphous layer of only about 1–2 nm in thickness is tightly coated onto the β-MnO_2 single crystal surface. This amorphous layer is conductive polypyrrole, which was *in situ* produced during the synthesis process. The observation of the ultrathin polypyrrole layer sheathed on the surface of β-MnO_2 nanorod in HRTEM is in good agreement with the previous FTIR analysis.

Formation mechanism

The crystal structure of β-MnO_2 is composed of individual chains of the [MnO_6] octahedral units, forming the one dimensional channel [1 × 1] structure (Fig. 3). The crystal structure and morphology of MnO_2 were reported to be dependent on synthetic conditions, reagents, concentrations, and pH of the solutions.[19] We found that, without adding H_2SO_4, the redox reaction between pyrrole monomers and Mn^{7+} was very slow even though the concentration of the two reagents was high. As we know, the oxidation capability of $KMnO_4$ is dependent on the pH of the solution. A small increase in acid concentration greatly increased the oxidation capability of $KMnO_4$, leading to a high growth rate of all crystal planes. Thus, adding H_2SO_4 and controlling its concentration are critical for the morphology of the final products. In the approach presented here, the proper control of the concentration of H_2SO_4 and its ratio to the concentration of $KMnO_4$ resulted in a fast elongation of $(1\bar{1}2)$ crystal plane while keeping the formation rates of other crystal planes low. The special advantage of our experiment design is that we chose an organic monomer, pyrrole, as a reducing reagent, which was then oxidized into insoluble polymer to hinder the further crystal growth of MnO_2. The schematic formation process is illustrated in Fig. 3. After all these factors work jointly, the unique hybrid composite can be produced in the form of ultrafine nanorod powders. This design principle might be useful in seeking a versatile synthetic route to growing other ultrafine 1D nanostructures of interest.

Electrochemical characterization

The MnO_2/polypyrrole nanorod composite powders were employed to fabricate supercapacitor electrodes, which were then characterized using cyclic voltammograms (CV). The representative CV curves measured with the electrodes at different scan rates in 1 M Na_2SO_4 are presented in Fig. 4. The quasi-rectangular shape of the CV curves demonstrates a remarkable capacitance characteristic of the electrodes. The lower scan rate leads to a pronounced rectangular shape and a higher capacitance value.

Charge–discharge performances at the current densities of 0.2, 0.5, 1, 2, 5, 10, and 20 A g^{-1} were measured on the MnO_2/polypyrrole nanorod composite electrode as shown in Fig. 5a and b. The charge and discharge curves are quite symmetrical at the current densities of 1 and 2 A g^{-1}, indicating an excellent capacitance behavior. At the higher rates of 5, 10, and 20 A g^{-1}, a small internal resistance (IR) drop is visible at the initial discharging stage (1.0–0.9 V). Such a small IR drop is not apparent at the lower rate range below 2 A g^{-1}. The specific capacitance of the electrode at different current density is calculated by $C = \dfrac{i \times \Delta t}{m \times \Delta V}$ from the discharge curves, where i is the constant discharge current, m is the mass of the active materials in the electrode, Δt is the discharge time, and ΔV is the potential drop during discharge. The specific capacitance value is 294 F g^{-1} for the MnO_2/polypyrrole nanorod composite electrode with an applied current density of 1 A g^{-1} in the potential range of 0–1.0 V. β-MnO_2 has a one dimensional channel [1 × 1] structure, which was usually regarded as not the desirable crystal structure for supercapacitor applications.[17,18] But the specific capacitance of the β-MnO_2/polypyrrole nanorod composite electrode here is comparable to 297 F g^{-1} of the best crystal structure, α-MnO_2, and is much better than 7 F g^{-1} of the β-MnO_2.[18] We attributed the surprising high performance of the β-MnO_2/polypyrrole nanorod to its ultra small size. When the size of β-MnO_2 decreases to very small (<10 nm in diameter),

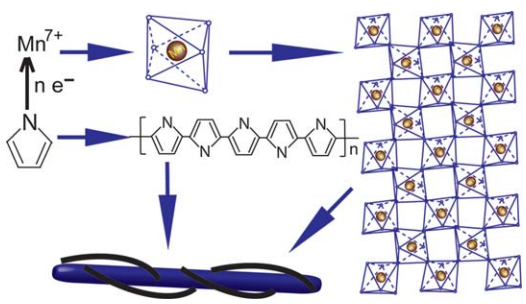

Fig. 3 Schematic of the formation process of the β-MnO_2/polypyrrole nanorod composite.

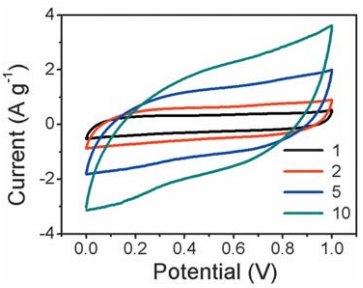

Fig. 4 (a) Cyclic voltammograms of the MnO_2/polypyrrole nanorod composite electrode in 1 M Na_2SO_4 at the scan rates of 1, 2, 5, and 10 mV s^{-1}, respectively.

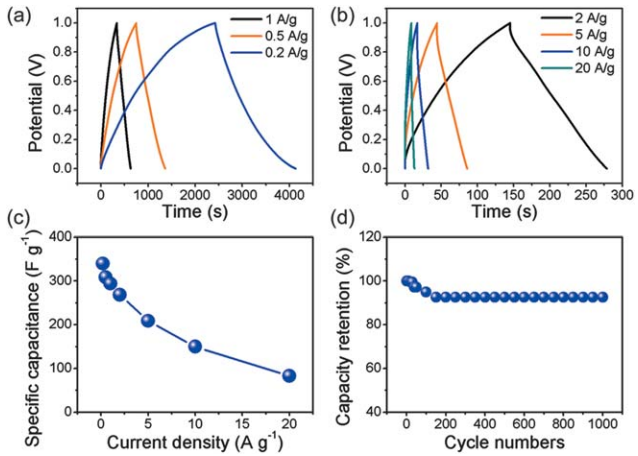

Fig. 5 Constant current charge/discharge curves of the β-MnO_2/polypyrrole nanorod composite electrode at different rates: (a) 0.2, 0.5, and 1 A g^{-1}; (b) 2, 5, 10, and 20 A g^{-1}. (c) Plot of specific capacitance as a function of current density. (d) Corresponding charge–discharge cycle.

almost all the Mn(IV) atoms are on the surface and subjected to be reduced upon intercalation of cations. Therefore, how the MnO_6 octahedra is arranged in ultra-fine nanorod β-MnO_2 is not so important as its 'bulk' counter partner. The further investigation of the effect of crystallographic structure of MnO_2 at ultra small regime on its specific capacitance will be an interesting subject.

The rate capability is another critical factor for evaluating the practical application of the MnO_2/polypyrrole nanorod composite electrode in supercapacitors. Fig. 5c shows the rate dependent specific capacitance calculated from the charge–discharge curves in Fig. 5a and b. An even higher specific capacitance value of 340 F g^{-1} was achieved if the charge/discharge rate was slowed down to 0.2 A g^{-1}. The specific capacitance of the MnO_2/polypyrrole nanorod composite electrode at high charge/discharge rates of 10 and 20 A g^{-1} decreases to the range of 83–150 F g^{-1}, indicating a little bit of aggregation of the ultrafine nanorod powder was occurred. The further investigation on the well dispersed and hieratically organized ultrafine nanorod powder is needed. But relative high capacitance of the β-MnO_2 still shows an attractive performance at high power density.

The electrochemical stability of the MnO_2/polypyrrole nanorod composite electrode was examined by chronopotentiometry at 5 A g^{-1} in the potential range of 0–1.0 V. Fig. 5d shows the retention of the specific capacitance of the prepared electrode with respect to charge–discharge cycle number. The specific capacitance of the MnO_2/polypyrrole nanorod composite electrode declined slightly in the first 150 cycles, but remained constant thereafter. The specific capacitance kept 92.6% after 1000 charge/discharge cycles.

Energy density (E) and power density (P) of the MnO_2/polypyrrole nanorod composite electrode were calculated from the following equations:

$$E = \frac{1}{2}C(\Delta V)^2 \quad (1)$$

$$P = \frac{E}{t} \quad (2)$$

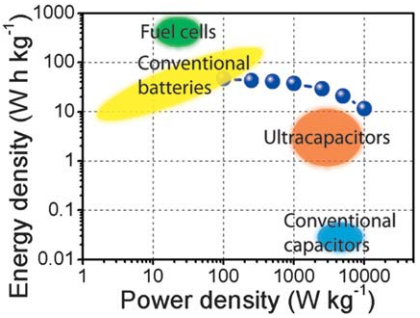

Fig. 6 Energy density as a function of power density for the β-MnO_2/polypyrrole nanorod composite electrode in a Ragone plot, added to the energy density—power density map for all existing energy storage systems for comparison.[26]

where E (W h kg^{-1}), C (F g^{-1}), ΔV (V), t (s), and P (W kg^{-1}) are energy density, specific capacitance, potential window of discharge, discharge time, and power density, respectively. Our data were compared with reference to the data from fuel cells, conventional batteries, conventional capacitors, and normal ultracapacitors,[26] as shown in Fig. 6. The MnO_2/polypyrrole nanorod composite electrode demonstrates a much higher energy density than conventional capacitors and normal ultracapacitors, while still keeps high power density, making it a promising electrode for fabricating supercapacitor devices.

Conclusions

In summary, we have developed a facile, simple, and effective approach to synthesizing ultrafine β-MnO_2/polypyrrole nanorod composite powders. The ultrafine β-MnO_2/polypyrrole nanorod composite electrode has demonstrated superior performance: (1) the specific capacitance reaches 294 F g^{-1} at a charge/discharge current density of 1 A g^{-1} in the 0–1.0 V potential window, which is surprisingly high compared with 7 F g^{-1} of other β-MnO_2 powders with larger size; (2) it can work at a high power density of 10 kW kg^{-1}, while still keeps a high energy density of 11.5 W h kg^{-1} and a high specific capacitance of 83 F g^{-1}. Our observation may encourage a revisit of the other good or even bad candidate active materials if we can decrease their size to extremely small scales. In addition, the proposed synthetic mechanism and the developed synthetic strategy may provide design guidelines in synthesizing other energy storage materials toward the ultrafine 1D nanostructure with diameter below 10 nm.

Acknowledgements

This work was supported by the U.S. Army Research Office under agreement/grant W911NF-07-1-0320 and the National Science Foundation (CMMI-0653651 and CMMI-0968843). The authors thank Dr Douglas Blom at the University of South Carolina EM Center for TEM technical support.

References

1 P. Simon and Y. Gogotsi, *Nat. Mater.*, 2008, **7**, 845.
2 E. Frackowiak and F. Beguin, *Carbon*, 2001, **39**, 937.
3 J. P. Zheng and T. R. Jow, *J. Electrochem. Soc.*, 1995, **142**, L6.

4 J. P. Zheng, P. J. Cygan and T. R. Jow, *J. Electrochem. Soc.*, 1995, **142**, 2699.
5 K. H. Chang and C. C. Hu, *Electrochem. Solid-State Lett.*, 2004, **7**, A466.
6 M. Toupin, T. Brousse and D. Belanger, *Chem. Mater.*, 2004, **16**, 3184.
7 M. M. Thackeray, *Prog. Solid State Chem.*, 1997, **25**, 1.
8 S. Trasatti, *Electrochim. Acta*, 1991, **36**, 225.
9 T. C. Liu, W. G. Pell and B. E. Conway, *Electrochim. Acta*, 1997, **42**, 3541.
10 S. Ardizzone, G. Fregonara and S. Trasatti, *Electrochim. Acta*, 1990, **35**, 263.
11 J. A. Yan, E. Khoo, A. Sumboja and P. S. Lee, *ACS Nano*, 2010, **4**, 4247.
12 L. H. Bao, J. F. Zang and X. D. Li, *Nano Lett.*, 2011, **11**, 1215.
13 S. Chen, J. W. Zhu, Q. F. Han, Z. J. Zheng, Y. Yang and X. Wang, *Cryst. Growth Des.*, 2009, **9**, 4356.
14 Y. Hou, Y. W. Cheng, T. Hobson and J. Liu, *Nano Lett.*, 2010, **10**, 2727.
15 R. Liu and S. B. Lee, *J. Am. Chem. Soc.*, 2008, **130**, 2942.
16 J. F. Zang, S. J. Bao, C. M. Li, H. J. Bian, X. Q. Cui, Q. L. Bao, C. Q. Sun, J. Guo and K. R. Lian, *J. Phys. Chem. C*, 2008, **112**, 14843.
17 O. Ghodbane, J. L. Pascal and F. Favier, *ACS Appl. Mater. Interfaces*, 2009, **1**, 1130.
18 S. Devaraj and N. Munichandraiah, *J. Phys. Chem. C*, 2008, **112**, 4406.
19 X. Wang and Y. D. Li, *J. Am. Chem. Soc.*, 2002, **124**, 2880.
20 J. H. Zhu, S. Y. Wei, L. Zhang, Y. B. Mao, J. Ryu, P. Mayinakuli, A. B. Karki, D. P. Young and Z. H. Guo, *J. Phys. Chem. C*, 2010, **114**, 16335.
21 P. Mavinakuli, S. Y. Wei, Q. Wang, A. B. Karki, S. Dhage, Z. Wang, D. P. Young and Z. H. Guo, *J. Phys. Chem. C*, 2010, **114**, 3874.
22 A. K. Cuentas-Gallegos and P. Gomez-Romero, *J. New Mater. Electrochem. Syst.*, 2005, **8**, 181.
23 Z. H. Guo, K. Shin, A. B. Karki, D. P. Young, R. B. Kaner and H. T. Hahn, *J. Nanopart. Res.*, 2009, **11**, 1441.
24 J. Li, L. Cui and X. G. Zhang, *Appl. Surf. Sci.*, 2010, **256**, 4339.
25 J. B. Schlenoff and H. Xu, *J. Electrochem. Soc.*, 1992, **139**, 2397.
26 S. Zurek, http://en.wikipedia.org/wiki/File:Supercapacitors_chart.svg.